E1-2005-46

A. Krása[1,a], F. Křížek[1], V. Wagner[1,b], A. Kugler[1],
V. Henzl[1], D. Henzlová[1], M. Majerle[1], J. Adam[1,2],
V. Bradnová[2], P. Čaloun[1,2], D. Chultem[2], V. G. Kalinnikov[2],
M. I. Krivopustov[2], A. A. Solnyshkin[2], V. I. Stegailov[2],
V. M. Tsoupko-Sitnikov[2], Ts. Tumendelger[2], S. I. Vasiliev[2]

NEUTRON PRODUCTION IN SPALLATION REACTIONS
OF 0.9 AND 1.5 GeV PROTONS
ON A THICK LEAD TARGET.
COMPARISON BETWEEN EXPERIMENTAL DATA
AND MONTE-CARLO SIMULATIONS

[1]Nuclear Physics Institute of the Academy of Sciences
 of Czech Republic, Řež, Czech Republic
[2]Joint Institute for Nuclear Research, Dubna, Russia
[a]E-mail: krasa@ujf.cas.cz
[b]URL: http://ojs.ujf.cas.cz/~wagner/transmutace/adtten.html

Краса А. и др.   E1-2005-46

Выход нейтронов из толстой свинцовой мишени в реакциях
расщепления протонами с энергией 0,9 и 1,5 ГэВ.
Сравнение экспериментальных результатов
с расчетами по программе MCNPX

Представлены результаты двух экспериментов, выполненных на синхрофазотроне и нуклотроне ОИЯИ. Релятивистские протоны с энергией 885 МэВ и 1,5 ГэВ взаимодействовали с массивной цилиндрической свинцовой мишенью. Измерялось пространственное и энергетическое распределение спалогенных нейтронов методом активации Al-, Au-, Bi-, Co- и Cu-фольг, размещенных на поверхности мишени и вблизи нее. Выход радионуклидов, образованных при пороговых реакциях в указанных фольгах, определялся анализом их гамма-спектров. Сравнение с расчетами, выполненными методом Монте-Карло, было проведено по двум программам: LAHET+MCNP и MCNPX.

Работа выполнена в Лаборатории ядерных проблем им. В. П. Джелепова ОИЯИ.

Krása A. et al.   E1-2005-46

Neutron Production in Spallation Reactions
of 0.9 and 1.5 GeV Protons on a Thick Lead Target.
Comparison between Experimental Data
and Monte-Carlo Simulations

This paper reports on two experiments performed at the Synchrophasotron/Nuclotron accelerator complex at JINR. Relativistic protons with energies 885 MeV and 1.5 GeV hit a massive cylindrical lead target. The spatial and energetic distributions of the neutron field produced by the spallation reactions were measured by the activation of Al, Au, Bi, Co, and Cu foils placed on the surface of the target and close to it. The yields of the radioactive nuclei produced by threshold reactions in these foils were determined by the analyses of their γ spectra. The comparison with Monte-Carlo based simulations was performed both with the LAHET+MCNP code and the MCNPX code.

The investigation has been performed at the Dzhelepov Laboratory of Nuclear Problems, JINR.

INTRODUCTION

Spallation reactions can be used to produce high neutron fluxes by bombarding a thick heavy metal target with a high-intensity relativistic proton beam. Recently, possible applications, such as accelerator-driven transmutation of nuclear waste [1], have increased the interest in spallation reactions and in the transport of the produced neutrons.

This study is a part of a complex research of Accelerator Driven Transmutation Technologies carried out by the collaboration of NPI ASCR (Řež) and JINR (Dubna) [2–5]. The experiments were carried out at the Synchrophasotron and the Nuclotron accelerators at the Veksler and Baldin Laboratory of High Energies (JINR). Relativistic protons interacting with a massive cylindrical lead target produced the spallation neutrons. The spatial and energetic distributions of the produced neutron field were measured by the activation of Al, Au, Bi, Co, and Cu foils placed on the surface of the target and close to it. The activity of the foils was then measured by the HPGe detectors at the Dzhelepov Laboratory of Nuclear Problems (JINR). The yields of the radioactive nuclei produced in these foils were calculated from their resulting γ spectra. The aim of performed experiments is to check the validity of the model descriptions and of the cross-section libraries used in the corresponding Monte-Carlo simulations of spallation reactions, and of the propagation of the produced high-energy neutrons through thick target.

There are several simulation codes and combinations of these codes describing spallation reactions, interactions of secondary particles, and the following neutron transport through the target material. They are based on the mathematical Monte-Carlo method, and they use various physical models of spallation reactions and cross-section libraries of neutron induced reactions with nuclei. All Monte-Carlo simulations were carried out by a combination of LAHET plus MCNP codes, and by MCNPX code. LAHET (Los Alamos High Energy Transport Code) [6] can model spallation reactions and transport of nucleons, pions, muons, antinucleons with energy $E \geqslant 20$ MeV. LAHET generates cross sections for individual processes. MCNP (Monte Carlo N-Particle Transport Code) [7] is able to model the transport of neutrons (and photons and electrons) in the energy range 10^{-11} MeV $\leqslant E \leqslant 20$ MeV. It uses libraries of evaluated data (such as ENDF/B-VI) as a source of the cross sections. MCNPX (MCNP eXtended) [8] improves and links the advantages of both LAHET and MCNP. MCNPX supports 34 particle types, the ability to calculate interaction probabilities directly with physical models for energies where tabular data are not available, and exploits new libraries of evaluated cross sections up to 150 MeV [9].

1

1. EXPERIMENTS

The first presented experiment was carried out at the Synchrophasotron. The beam of 885 MeV protons hits a multi-section cylindrical lead target (diameter $d = 9.6$ cm, total length $l = 50$ cm) surrounded by a box of expanded polystyrene ($17.6 \times 17.1 \times 52.6$ cm^3) as a thermal isolation to allow the measurement of the heat production. The whole set-up was surrounded by a biological shielding consisted of a container ($106 \times 106 \times 111$ cm^3) filled with granulated polyethylene with admixture of boron and 0.1-cm Cd layer on inner walls (used for absorption of thermal neutrons). The front and the back ends of the set-up were without any shielding, see Fig. 1. Polyethylene moderated and partly scattered the high-energy neutrons outgoing from the set-up, and created quite homogeneous field of neutrons with energy 1 eV $\leqslant E \leqslant 0.1$ MeV inside the container, see Fig. 5. Herewith, the moderator disallowed the study of spatial distribution of low-energy neutrons produced in the spallation target. The next element of a shielding was a lead wall of 10 cm thick, which was placed at the distance of 10 cm behind the target.
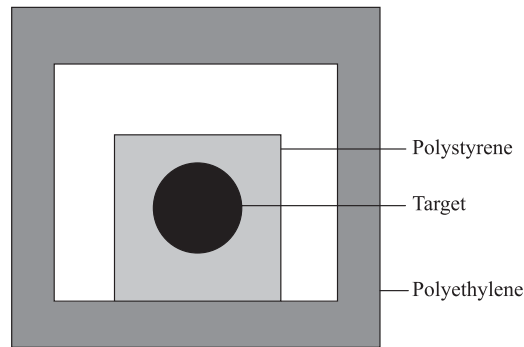

Fig. 1. A scheme of «Pb» set-up (proton eye's view)

The course of the irradiation is shown in Fig. 2. The error of incident proton beam energy is estimated at the level of 0.5%. The irradiation continued for $t_{irr} = 7369$ s, and the total number of beam protons was $I(p) = (3.5 \pm 0.2) \cdot 10^{13}$ as determined by activation of beam monitors. The primary protons with an energy of 885 MeV were stopped after passing about 46 cm in the target [10]. Further part of the target was influenced only by the shower of secondary particles, which consists mainly of neutrons.

The second presented experiment was performed at the superconducting, strong focusing synchrotron named Nuclotron [11, 12] with proton energy of
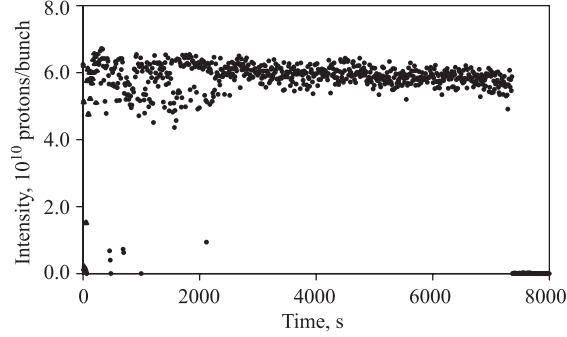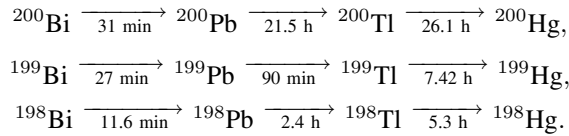
2

Fig. 2. Course of irradiation with 885 MeV protons

1.5 GeV on the «Energy plus Transmutation» installation [4]. This installation using a Pb/U assembly consisted of a 43 kg cylindrical lead target (d = 8.4 cm, l = 48 cm) plus 206.4 kg natural uranium blanket with hexagonal cross section (side length of 16.1 cm) consisted of four sections (separated by 0.8-cm empty intervals), each containing 30 uranium rods. Each rod (d = 3.6 cm, l = 10.4 cm, m = 1.72 kg, $\rho = 15.8$ g/cm^3) was sealed in an aluminium cover of 0.165 cm thick. The set-up was surrounded by the same container as in the first case, see Fig. 3.

The course of the irradiation is shown in Fig. 4. The irradiation continued for $t_{\mathrm{irr}} = 44584$ s, and the total number of beam protons was $I(p) = (1.14 \pm 0.06) \cdot 10^{13}$ as determined by activation of beam monitors. The range of protons with an energy of 1500 MeV is about 94 cm [10], and a part of primary protons flew through the whole target. Details and description of other radiochemical techniques, using solid state nuclear track detectors, etc., are discussed in detail in [13].

The spatial distribution of the produced neutron field was measured by the neutron activation analysis method using activation foils of ^{27}Al, ^{197}Au, ^{209}Bi, and ^{59}Co placed on the surface of and next to the target. In the process of irradiation, the stable isotopes were transmuted by (n, γ), (n, α), (n, xn, yp) reactions into radioactive ones. Studied neutron-induced reactions both with a threshold in neutron energy and without it are shown in Table 1 and Fig. 6. Yields of isotopes with too short half-lives were determined with help of γ transitions from decays of their daughter products, e.g.,

$$^{200}\mathrm{Bi} \xrightarrow[31\ \mathrm{min}]{} {}^{200}\mathrm{Pb} \xrightarrow[21.5\ \mathrm{h}]{} {}^{200}\mathrm{Tl} \xrightarrow[26.1\ \mathrm{h}]{} {}^{200}\mathrm{Hg},$$

$$^{199}\mathrm{Bi} \xrightarrow[27\ \mathrm{min}]{} {}^{199}\mathrm{Pb} \xrightarrow[90\ \mathrm{min}]{} {}^{199}\mathrm{Tl} \xrightarrow[7.42\ \mathrm{h}]{} {}^{199}\mathrm{Hg},$$

$$^{198}\mathrm{Bi} \xrightarrow[11.6\ \mathrm{min}]{} {}^{198}\mathrm{Pb} \xrightarrow[2.4\ \mathrm{h}]{} {}^{198}\mathrm{Tl} \xrightarrow[5.3\ \mathrm{h}]{} {}^{198}\mathrm{Hg}.$$
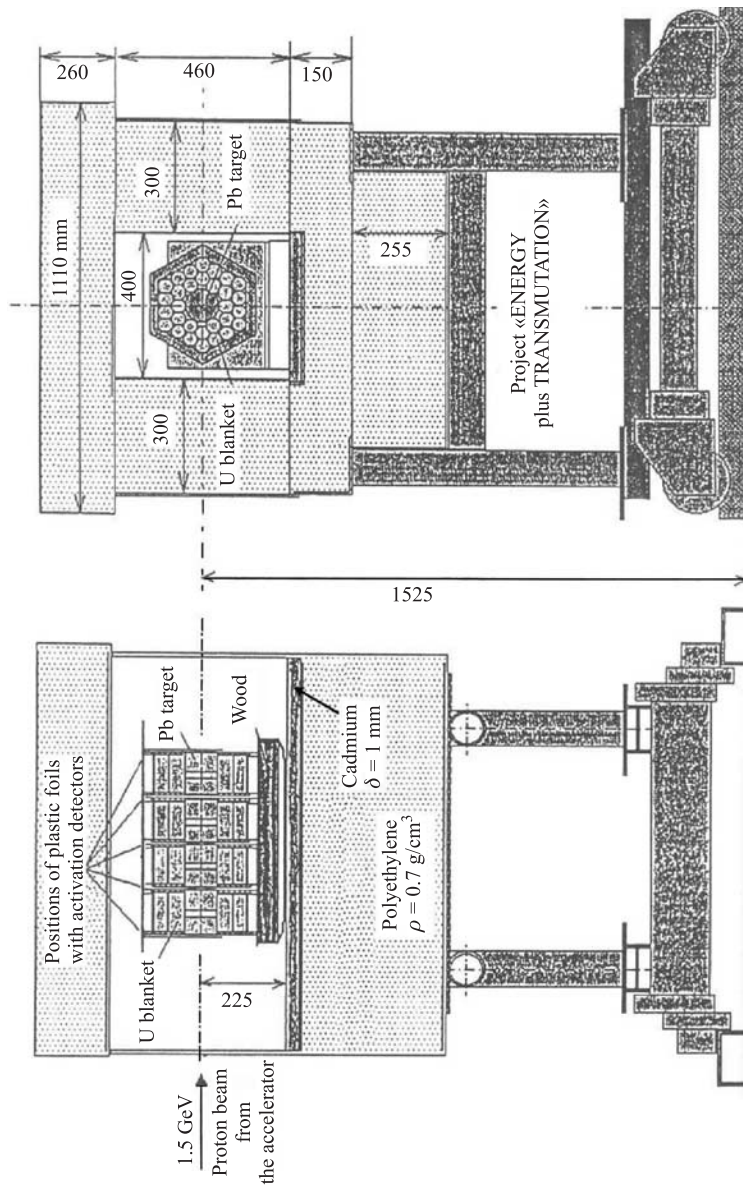
3

Fig. 3. «Energy plus Transmutation» «Pb/U» set-up
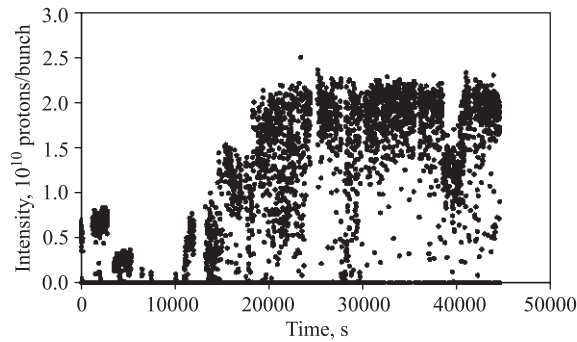
4

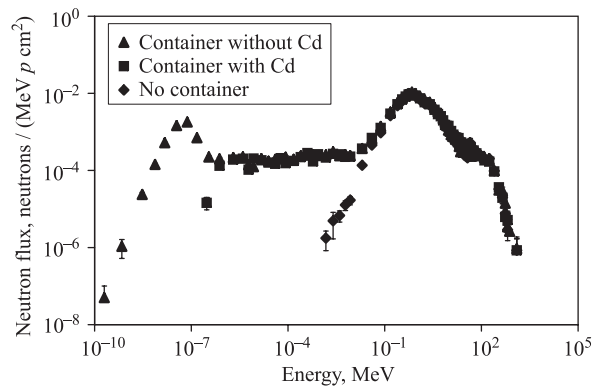Fig. 4. Course of irradiation with 1.5 GeV protons

Fig. 5. Influence of container and Cd layer on neutron spectra on the top of the uranium blanket, 11.8 cm from the front, inside the shielding container with the «Energy plus Transmutation» set-up (MCNPX simulation)

The advantage of the activation-analysis method is that detectors can be simple and can have arbitrary size (used foils had 2×2 cm^2 in size with approximately 50 μm in thickness), it is possible to place them at any position of the set-up, they are not responsive to γ rays, temperature, pressure. The disadvantage is that the measured quantity is the amount of produced radioactive nuclei, from which it is not always straightforward to determine the incident neutron field. Problem can be also in incomplete libraries of cross sections.

In the first experiment the foils were located closely above the target (exactly 5 cm above the target axis), closely above the polystyrene box (9.3 cm above the
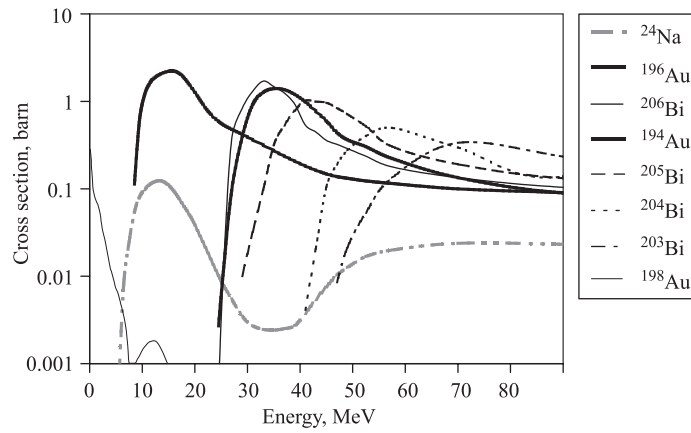
5

Fig. 6. Examples of cross sections of reactions studied by the activation analysis method (single items in legend are sequenced in line with increasing threshold energy)

target axis) and on the right side of the polystyrene box (9.1 cm to the right from the target axis). The foils were located side by side all along the target in order to determine the spatial distribution of the neutron field, see Fig. 7.
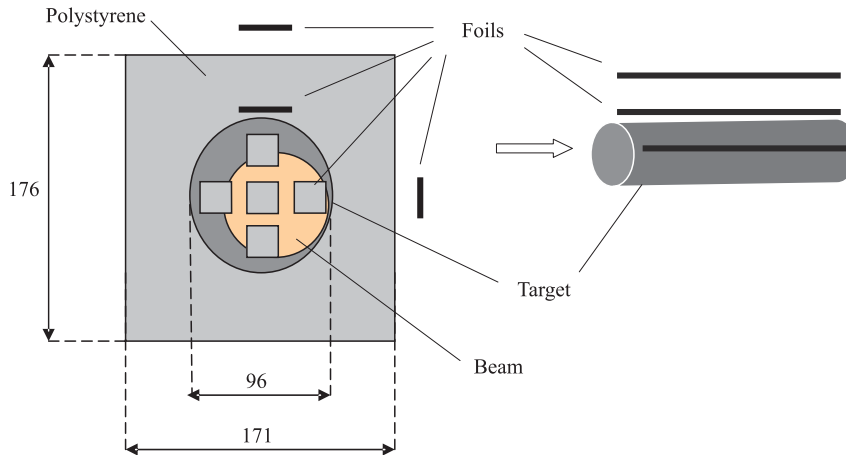

Fig. 7. A scheme of placement of activation foils at the «Pb» set-up

In the second experiment the foils were placed at a radial distance of 3 cm from the target axis at five longitudinal distances of 0.0, 11.8, 24.0, 36.2, 48.4 cm

6

Table 1. **Examples of threshold and nonthreshold reactions studied by the activation analysis method (calculated with help of [14] based on [15] tables)**

Reaction	Threshold energy, MeV	Half-life of pro-duct	Reaction	Threshold energy, MeV	Half-life of pro-duct
$^{27}\mathrm{Al}(n,\alpha)^{24}\mathrm{Na}$	5.5	14.959 h	$^{197}\mathrm{Au}(n,\gamma)^{198}\mathrm{Au}$	—	2.69517 d
$^{209}\mathrm{Bi}(n,4n)^{206}\mathrm{Bi}$	22.6	6.243 d	$^{197}\mathrm{Au}(n,2n)^{196}\mathrm{Au}$	8.1	6.183 d
$^{209}\mathrm{Bi}(n,5n)^{205}\mathrm{Bi}$	29.6	15.31 d	$^{197}\mathrm{Au}(n,3n)^{195}\mathrm{Au}$	14.8	186.10 d
$^{209}\mathrm{Bi}(n,6n)^{204}\mathrm{Bi}$	38.1	11.22 h	$^{197}\mathrm{Au}(n,4n)^{194}\mathrm{Au}$	23.2	1.584 d
$^{209}\mathrm{Bi}(n,7n)^{203}\mathrm{Bi}$	45.2	11.76 h	$^{197}\mathrm{Au}(n,5n)^{193}\mathrm{Au}$	30.2	17.65 h
$^{209}\mathrm{Bi}(n,8n)^{202}\mathrm{Bi}$	54.0	1.72 h	$^{197}\mathrm{Au}(n,6n)^{192}\mathrm{Au}$	38.9	4.94 h
$^{209}\mathrm{Bi}(n,9n)^{201}\mathrm{Bi}$	61.4	1.8 h	$^{197}\mathrm{Au}(n,7n)^{191}\mathrm{Au}$	45.7	3.18 h
$^{209}\mathrm{Bi}(n,10n)^{200}\mathrm{Bi}$	70.8	36.4 m	$^{59}\mathrm{Co}(n,\gamma)^{60}\mathrm{Co}$	—	5.271 y
$^{209}\mathrm{Bi}(n,11n)^{199}\mathrm{Bi}$	78.4	27 m	$^{59}\mathrm{Co}(n,2n)^{58}\mathrm{Co}$	10.6	70.82 d
$^{209}\mathrm{Bi}(n,12n)^{198}\mathrm{Bi}$	87.9	10.3 m	$^{59}\mathrm{Co}(n,3n)^{57}\mathrm{Co}$	19.4	271.79 d
$^{59}\mathrm{Co}(n,4n)^{56}\mathrm{Co}$	30.9	77.27 d	$^{59}\mathrm{Co}(n,5n)^{55}\mathrm{Co}$	41.2	17.53 h

from the target front and also at a longitudinal distance of 11.8 cm from the target front at four radial distances of 3.0, 6.0, 8.5, 13.5 cm from the target axis, see Fig. 8.
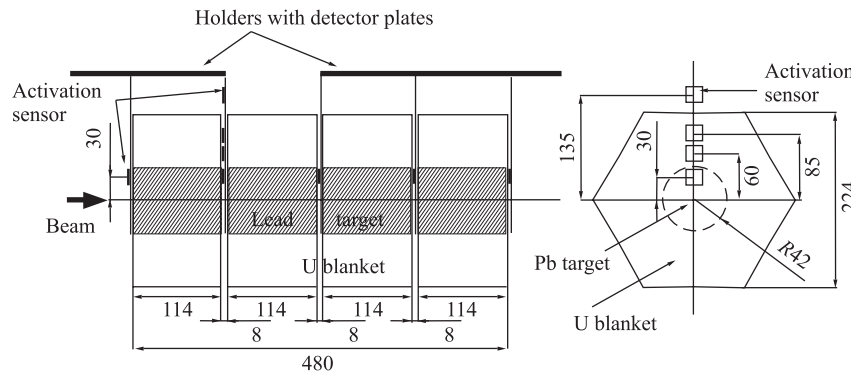

Fig. 8. A scheme of placement of activation foils at the «Pb/U» set-up

The beam geometry and total beam flux were also determined by the activation analysis method. The beam geometry was studied with the use of high-energy proton reactions on $^{\mathrm{nat}}\mathrm{Cu}$ and $^{197}\mathrm{Au}$ (production of $^{48}\mathrm{V}$, $^{52}\mathrm{Mn}$, $^{58}\mathrm{Co}$, $^{44m}\mathrm{Sc}$, $^{47}\mathrm{Sc}$, $^{191}\mathrm{Pt}$, $^{74}\mathrm{As}$, $^{182}\mathrm{Ta}$). A group of five Cu and Au foils (2×2 cm^2 in size with approximately 50 μm in thickness) was placed closely in front of the target and the yields in different foils were compared. Based on the trace of the beam in a Polaroid foil, three assumptions were used: the central foil is fully covered,

7

the proton distribution is homogeneous, the beam has circular cross section. For example, in the first experiment, we found out that the beam was shifted (0.8 ± 0.3) cm down and (0.8 ± 0.3) cm right from the target axis and that the beam radius was (3.5 ± 0.3) cm, see Fig. 7.
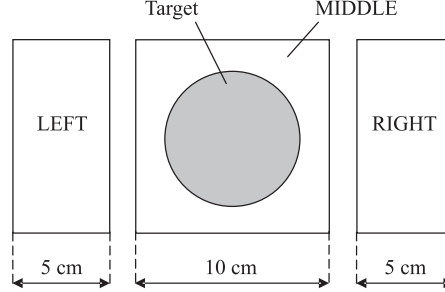

Fig. 9. A scheme of position of the beam monitors at the «Pb» set-up

The total beam intensity was determined by activation of beam monitors (composed of 10×10 cm^2 Cu foils with a thickness of 25 μm, and Al foils with a thickness of 100 μm) placed at the distance of 30 cm ahead of the target. In particular, the yields of the reactions ^{27}Al$(p, 3pn)^{24}$Na, ^{27}Al$(p, X)^7$Be, and ^{nat}Cu$(p, X)^{24}$Na were measured. The corresponding cross sections were acquired by interpolation using values from [26, 27]:

$$\sigma_{885}(^{27}\text{Al}(p, 3pn)^{24}\text{Na}) = (10.7 \pm 0.5) \text{ mb},$$

$$\sigma_{885}(^{nat}\text{Cu}(p, X)^{24}\text{Na}) = (0.78 \pm 0.04) \text{ mb},$$

$$\sigma_{885}(^{27}\text{Al}(p, X)^7\text{Be}) = (6.90 \pm 0.12) \text{ mb},$$

$$\sigma_{1500}(^{27}\text{Al}(p, 3pn)^{24}\text{Na}) = (10.01 \pm 0.11) \text{ mb},$$

$$\sigma_{1500}(^{nat}\text{Cu}(p, X)^{24}\text{Na}) = (2.3 \pm 0.2) \text{ mb},$$

$$\sigma_{1500}(^{27}\text{Al}(p, X)^7\text{Be}) = (8.86 \pm 0.12) \text{ mb}.$$

According to [24], there can be a problem with competitive reaction ^{27}Al$(n, \alpha)^{24}$Na, which can be caused by neutrons evaporated from the target in the direction against the beam. Considering their flux decreases as the inverse square of the distance from the target, beam monitors were placed at the distance of 30 cm from the target front, which is sufficient to screen backscattered neutrons. MCNPX calculated share of neutrons in the yield of ^{24}Na in the Al beam monitors is 4%. Similar contribution of 5% was measured by side monitors, see Fig. 9. This contribution was subtracted from the total yield in the central foil.

For example, in the first experiment, the total proton flux determined by the activation was $(3.5 \pm 0.2)\cdot 10^{13}$ (the error includes statistic and systematic errors of the applied cross sections, the calibration and the thickness of monitors).

The activity of the irradiated foils was measured by two HPGe γ-spectrometers by EG&G Ortec and Canberra companies. The coaxial GMX-20190-P detector had relative efficiency of 28.3% and energy resolution (FWHM of ^{60}Co at 1.33 MeV) of 1.90 keV, the coaxial GR1819-7600SL detector had relative efficiency of 18% and energy resolution of 1.90 keV. Measurements were taken in near geometries because of a low activity of the samples; the distance from the Ortec detector endcap was $d = 1.3$ cm and the distance from the Canberra detector endcap was $d = 0.4$ cm. Each foil was measured a few times in order to identify isotopes with different half-lives. Altogether, more than 150 (30) foils were measured and approximately 400 (100) γ-ray spectra were analyzed in the first (second) experiment (respectively).

The measured γ spectra of irradiated foils, covering region approximately from 50 up to 3500 keV, were processed by the DEIMOS32 code [17], that provides a Gaussian fit of γ peaks taking into account the background fitted with a parabola. The acquired areas were corrected for coincidence summing effects, for a peak efficiency of the HPGe detector, and for decay during irradiation and measurement. The yields (i.e., number of activated nuclei per one gram of activated material and per one incident proton) of the corresponding radioactive nuclei were determined according to the relation

$$N_{\text{yield}} = \frac{S_\gamma(E)}{I_\gamma(E)\epsilon_p(E)\text{COI}} \frac{t_{\text{real}}}{t_{\text{live}}} \frac{1}{mI(\text{p})} \frac{\exp(\lambda t_0)}{[1 - \exp(-\lambda t_{\text{real}})]} \frac{\lambda t_{\text{irr}}}{[1 - \exp(-\lambda t_{\text{irr}})]}, \tag{1}$$

where $S_\gamma(E)$ is fitted area of peak of γ transition with energy E; $I_\gamma(E)$ is intensity of this γ transition per decay; $\epsilon_p(E)$ is detector efficiency; COI is coincidence correction factor (see next paragraph); t_{real} is real time of measurement; t_{live} is live time of measurement; m is mass of a foil; $I(p)$ is total proton flux; t_0 is time from the end of the irradiation until the beginning of the measurement; t_{irr} is time of irradiation; $\lambda = \frac{\ln 2}{T_{1/2}}$ is disintegration constant. The relation between experimental yield $N_{\text{yield}}(E)$ and neutron flux can be derived with use of Fredholm's equation as follows:

$$N_{\text{yield}} = \frac{1}{A_r m_u I(p)} \int_0^\infty \Phi(E_n)\sigma(E_n)\text{dE}_\text{n}, \tag{2}$$

where A_r is specific atomic mass of a chemical element from which the foil is made, m_u is unified atomic mass unit ($m_u = 1.66 \cdot 10^{-27}$ kg). Integration of product of neutron flux $\Phi = \Phi(E_n)$ neutron$\cdot$(MeV$\cdot$proton$\cdot$cm$^2)^{-1}$ and cross section $\sigma = \sigma(E_n)$ of corresponding reaction is made over neutron energy E_n.

Table 2. **Energies and absolute intensities of calibration standards (taken from [20]); calculated COI factors for used geometries at both detectors**

Isotope	E, keV	I_γ, %	COI (Ortec)	COI (Canberra)	Isotope	E, keV	I_γ, %	COI (Ortec)	COI (Canberra)
^{60}Co	1173.2	99.97	0.92	0.93	^{152}Eu	1212.9	1.42	0.90	0.92
^{60}Co	1332.5	99.98	0.91	0.93	^{152}Eu	1299.1	1.63	0.90	0.92
^{57}Co	122.1	85.60	1.00	1.00	^{152}Eu	1408.0	21.01	0.99	1.00
^{57}Co	136.5	10.68	1.00	1.00	^{154}Eu	123.1	40.79	0.90	0.92
^{133}Ba	81.0	34.06	0.93	0.94	^{154}Eu	247.9	6.95	0.88	0.90
^{133}Ba	276.4	7.16	0.99	0.99	^{154}Eu	591.8	4.99	0.88	0.90
^{133}Ba	302.9	18.33	1.00	1.00	^{154}Eu	723.3	20.22	0.90	0.92
^{133}Ba	356.0	62.05	1.00	1.00	^{154}Eu	756.8	4.57	0.88	0.90
^{133}Ba	383.8	8.94	1.00	1.00	^{154}Eu	873.2	12.27	0.90	0.92
^{88}Y	898.0	93.70	0.92	0.94	^{154}Eu	996.3	10.6	0.92	0.94
^{88}Y	1836.1	99.20	0.91	0.93	^{154}Eu	1004.8	18.01	0.98	0.98
^{137}Cs	661.7	85.1	1.00	1.00	^{154}Eu	1274.4	35.19	0.99	0.99
^{152}Eu	121.8	28.37	0.90	0.93	^{154}Eu	1596.5	1.80	1.27	1.20
^{152}Eu	244.7	7.53	0.91	0.93	^{228}Th	238.6	43.5	1.00	1.00
^{152}Eu	295.9	0.447	0.88	0.91	^{228}Th	241.1	4.10	1.00	1.00
^{152}Eu	344.3	26.57	0.93	0.94	^{228}Th	277.4	2.30	0.84	0.87
^{152}Eu	367.8	0.816	0.90	0.92	^{228}Th	300.1	3.28	1.00	1.00
^{152}Eu	411.1	2.24	0.85	0.86	^{228}Th	549.8	0.114	1.00	1.00
^{152}Eu	778.9	12.94	0.91	0.92	^{228}Th	583.2	30.6	0.89	0.91
^{152}Eu	867.4	4.25	0.90	0.92	^{228}Th	727.3	6.58	0.97	0.98
^{152}Eu	964.1	14.61	0.96	0.97	^{228}Th	860.6	4.50	0.80	0.84
^{152}Eu	1085.8	10.21	1.00	1.00	^{228}Th	1620.7	1.49	1.01	1.01
^{152}Eu	1089.7	1.73	0.92	0.93	^{228}Th	2614.5	35.86	0.89	0.91
^{152}Eu	1112.1	13.64	1.00	1.00					

Calibration of detector efficiency was performed with the use of standard calibration point-like sources (dimensions in order of tenths of mm) ^{133}Ba (with relative error of reference activity 2.0%), ^{57}Co (1.8%), ^{60}Co (1.7%), ^{137}Cs (2.0%), ^{152}Eu (2.0%), ^{154}Eu (2.0%), ^{88}Y (1.7%), ^{228}Th (1.5%) (and daughter products) with several gamma lines ranging from 80 up to 2700 keV, see Table 2. All necessary corrections on possible coincidence summing effects were done and they are included in COI correction factor [18] in Eq. (1), see also Table 2. COI depends on the full-energy peak efficiency $\epsilon_p(E)$ (i.e., the detector ability to detect the total energy of the γ ray), and the total efficiency $\epsilon_t(E)$ (i.e., the detector ability to detect such a part of the γ-ray energy which is higher than detector resolution). For example, for used geometry at Ortec detector, the peak efficiency curve $\epsilon_p(E)$ (fitted for different ranges with a polynomial function of 3rd order, and with a linear function; of course, in logarithmic scale), and the curve of photofraction $R = \epsilon_p(E)/\epsilon_t(E)$ [19] (fitted with polynomial function of 2nd order in logarithmic scale) are shown in Fig. 10.
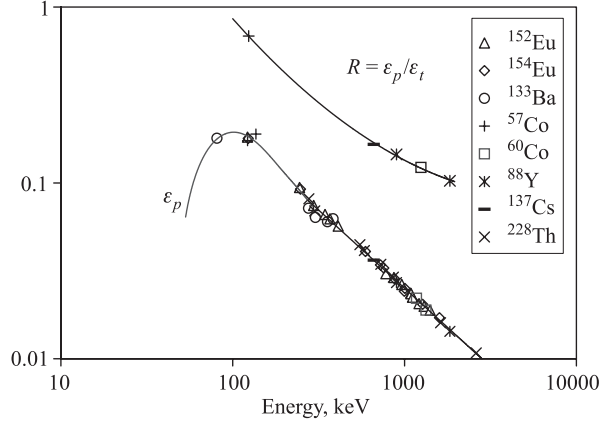
10

Fig. 10. The curve of peak efficiency $\epsilon_p(E)$ and the curve of photofraction $R = \epsilon_p(E)/\epsilon_t(E)$ (Ortec detector, $d = 1.3$ cm)

2. EXPERIMENTAL RESULTS

The yields in units (g^{-1} proton^{-1}) of radioactive isotopes produced in Al, Au, Bi, and Co foils are presented as a function of the position along the target in Figs. 12–16, 18, 20, 22, and as a function of radial distance from the target axis in Figs. 17, 19, 21, 23. Errors in figures are only statistical errors. Systematic errors, such as an inaccuracy of the position of foils, contribute about next 5%.

Neutrons produce the main part of radioactive nuclei. Most of them are evaporated neutrons which are emitted isotropically in spallation reactions [25]. The shape of the longitudinal distribution reflects the interplay of two main processes. First, the spallation cross section of protons decreases along the target in relation with the decrease in the primary proton energy due to the ionization looses. Second, the intensity of the primary proton beam decreases as well as part of the protons is scattered out. Consequently, the maximum intensity of the fast neutron field is shifted from the centre to the target's front — to the region between 7–11 cm from the target forehead.

The radial distributions swiftly decrease with the radial distance from the target axis. This agrees with the concept that the intensity of neutron flux falls down with growing perpendicular distance from the target axis.

The production maximum of isotopes ^{198}Au and ^{60}Co is evidently not so sharp in comparison with those in threshold reactions (in longitudinal as well as in radial distributions). Also the ratios of production ^{198}Au/^{194}Au and ^{198}Au/^{196}Au are unambiguously increasing at the end of the target, see Fig. 11. The reason

11
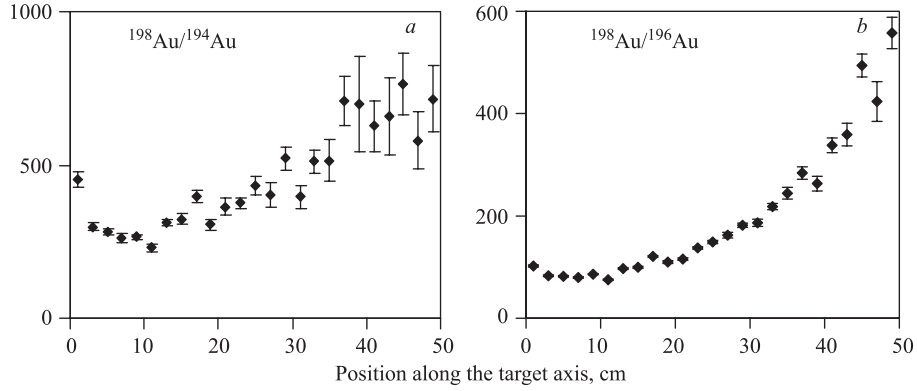
Fig. 11. Ratios of yields of ^{198}Au/^{194}Au (*a*) and ^{198}Au/^{196}Au (*b*) («Pb» set-up, 5 cm above the target axis)
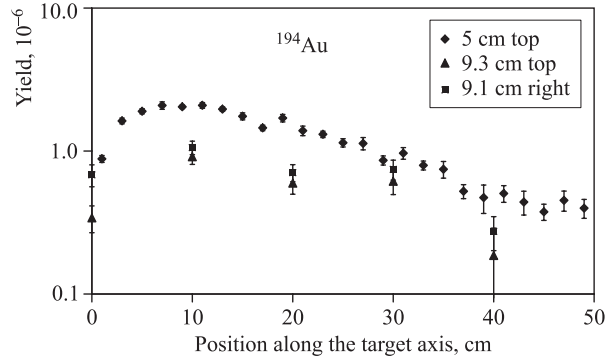
Fig. 12. Longitudinal distributions of yields of ^{194}Au («Pb» set-up)

can be the different behaviour of cross sections of neutron capture (production of ^{198}Au and ^{60}Co) in comparison with cross sections of threshold reactions (production of other isotopes). These ratios can be interpreted as increase of relative amount of low-energy neutrons in neutron field spectrum at the end of the target. The shielding (and the uranium blanket) partly moderated and scattered outgoing neutrons back. Herewith, quite homogeneous field of low-energy neutrons was created and this field gives constant contribution to the production of ^{198}Au and ^{60}Co in the whole set-up, that explains roughly flat shape of their distributions.

12
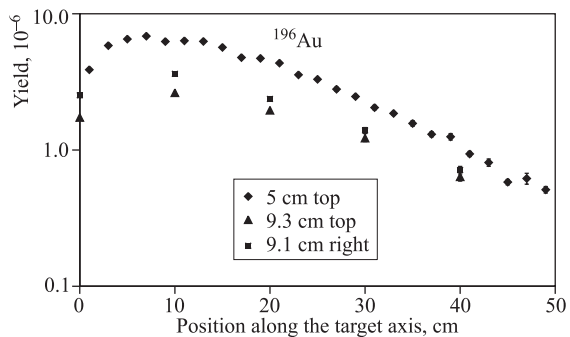
Fig. 13. Longitudinal distributions of yields of ^{196}Au («Pb» set-up)
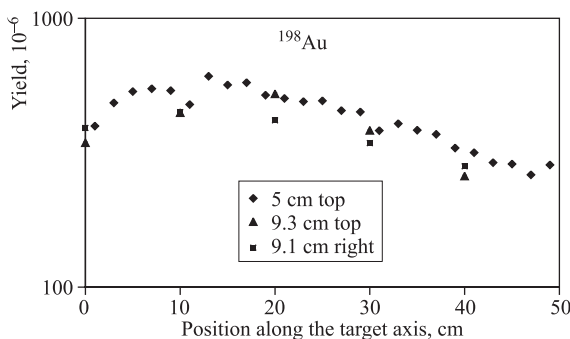
Fig. 14. Longitudinal distributions of yields of ^{198}Au («Pb» set-up)
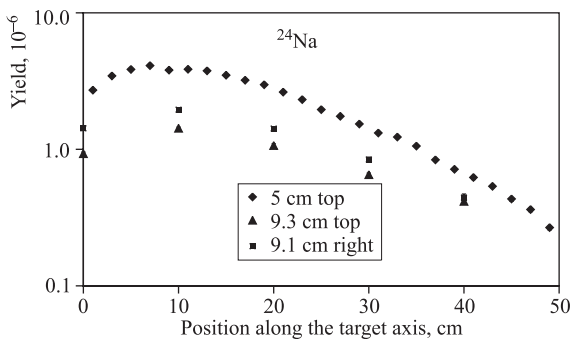
Fig. 15. Longitudinal distributions of yields of ^{24}Na («Pb» set-up)

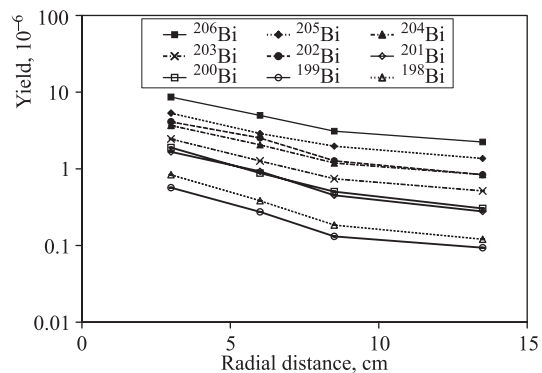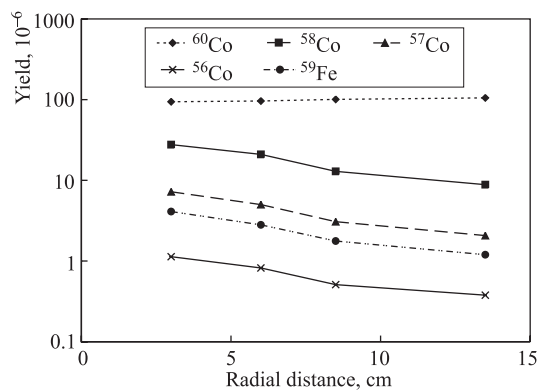Ratios between yields at the front and at the end of the target as a function of the reaction threshold energy are shown in Fig. 24. All dependencies fall down with growing threshold energy. Thus, we can conclude that the resulting

13
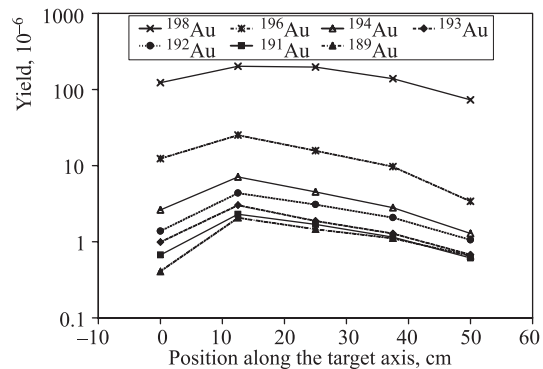
Fig. 16. Longitudinal distributions of yields of $^{198-189}$Au («Pb/U» set-up)
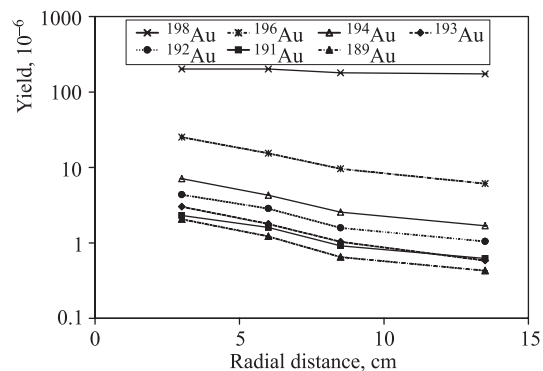
Fig. 17. Radial distributions of yields of $^{198-189}$Au («Pb/U» set-up)
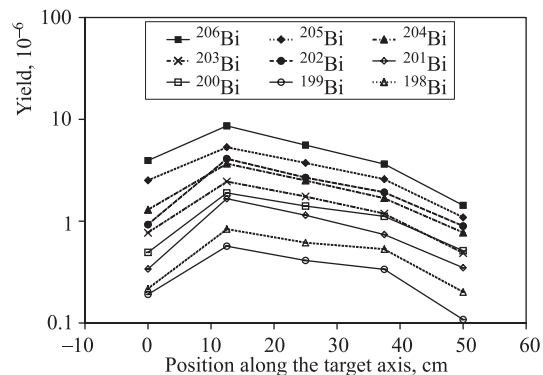
Fig. 18. Longitudinal distributions of yields of $^{206-198}$Bi («Pb/U» set-up)

14

Fig. 19. Radial distributions of yields of $^{206-198}$Bi («Pb/U» set-up)
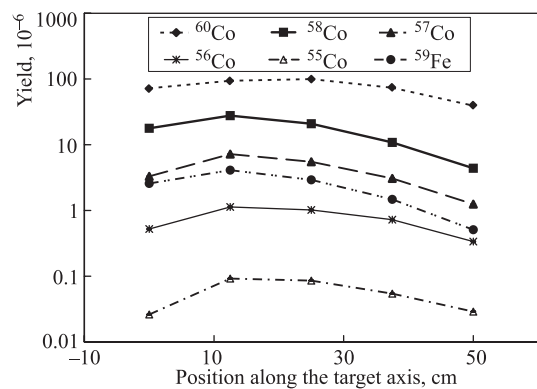
Fig. 20. Longitudinal distributions of yields of $^{60-55}$Co («Pb/U» set-up)
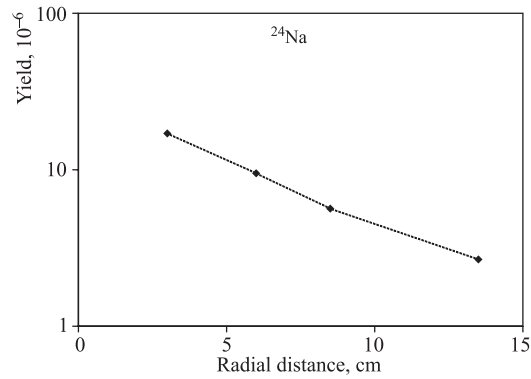

Fig. 21. Radial distribution of yields of $^{60-56}$Co («Pb/U» set-up)

15
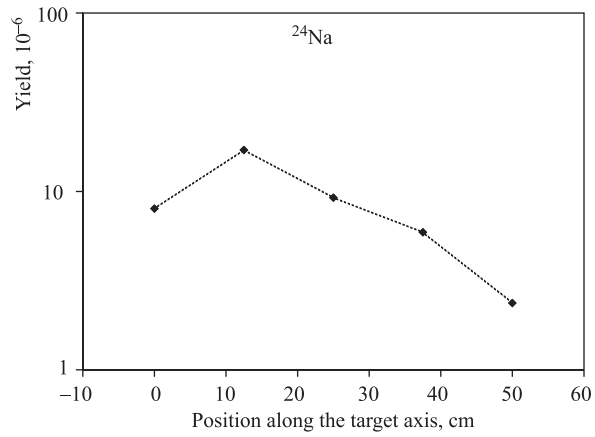
Fig. 22. Longitudinal distribution of yields of ^{24}Na («Pb/U» set-up)

Fig. 23. Radial distribution of yields of ^{24}Na («Pb/U» set-up)

experimental neutron spectrum is harder at the end of the target than at its front.

Ratios between yields at radial distances of 13.5 and 3.0 cm in the direction perpendicular to the target axis as a function of the reaction threshold energy are shown in Fig. 25. In contrast to Fig. 24, these ratios are not significantly dependent on threshold energy. The neutron spectrum was more or less the same in both positions.
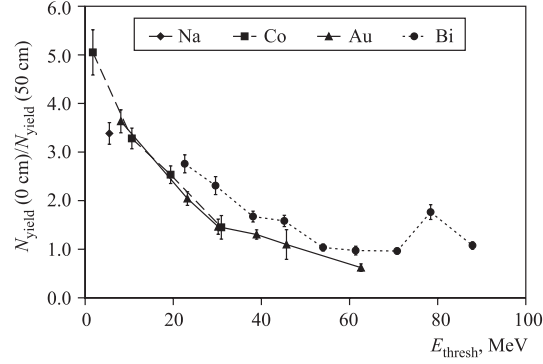
16

Fig. 24. Ratios of yields inside the Pb target (at a radial distance $R = 3$ cm) at the front and at the end of the target as a function of the reaction threshold energy («Pb/U» set-up)
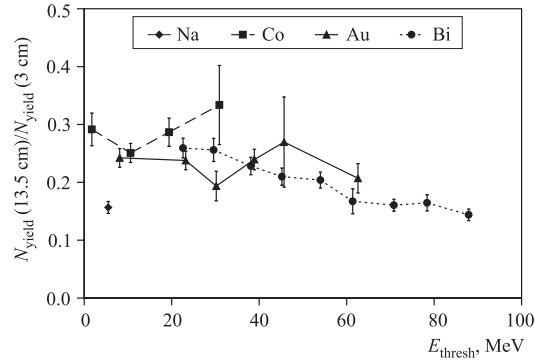

Fig. 25. Ratios of yields in the first gap (at a longitudinal distance $R = 11.8$ cm) at radial distances of 13.5 and 3.0 cm from the target axis as a function of the reaction threshold energy («Pb/U» set-up)

3. SIMULATIONS

The processing of the experimental data was accompanied by simulations of the neutron production in spallation reactions. Simulations were performed by MCNPX 2.3.0 code and by combination of LAHET 2.7 plus MCNP4B codes. The simulation of the course of the spallation reaction consists from three stages:

• *intranuclear cascade stage* was calculated using Bertini INC model [21], where the interaction between impinging particle and nucleons is described as a sequence of binary collisions. Collisions between cascade nucleons are not allowed. The nuclear density distribution is approximated by a step-function distribution. The densities in three regions with constant density are fitted to the folded Saxon–Woods shape;

17

• *pre-equilibrium stage* was simulated by MPM (Multistage Pre-equilibrium Exciton Model), an exciton is either nucleon excited above the Fermi level or vacancy under the Fermi level. The energy equalization occurs by two-particle interactions, the emission of particles and fragments is considered;

• *equilibrium stage* in which the particle evaporation or fission of thermally equilibrated nucleus happen. The equilibrium decay is described by evaporation models based on statistical approaches. The probability of the nucleus decay into certain channel depends on state densities in final channel and on probability of passage through the energy barrier.

Calculations were done in two steps:

• calculation of neutron $\Phi_n(E)$ and proton $\Phi_p(E)$ energy spectra, see Fig. 26;

• calculation of the yields of produced nuclei by convolution of these spectra with the corresponding cross sections $\sigma_n(E)$ and $\sigma_p(E)$, respectively, see Eq. (3).

These cross sections were partly taken (up to 30 MeV for Au, up to 20 MeV for Al) from ENDF/B-VI library [22], for higher energies (if it was in agreement with ENDF/B-VI in lower energies and was possible to link together) were taken from EXFOR/CSISRS [23] and mostly calculated using LAHET.

The simulated yields of produced nuclei were determined according to the following equation:

$$N_{\text{yield}}(r,z) = \frac{1}{A_r m_u I(p)_{\text{sim}}} \int_0^\infty [\Phi_n(E,r,z)\sigma_n(E) + \Phi_p(E,r,z)\sigma_p(E)]dE, \quad (3)$$

where A_r is specific atomic mass of a chemical element from which the foil is made; m_u is unified atomic mass unit; and $I(p)_{\text{sim}}$ is number of simulated
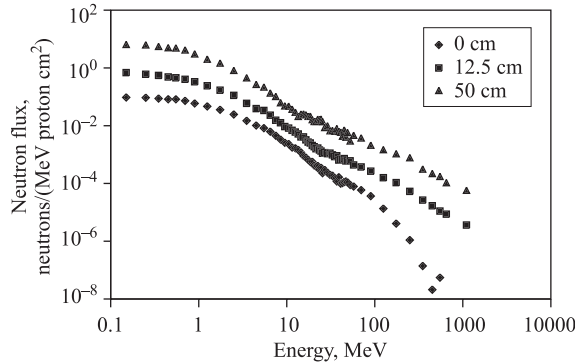

Fig. 26. MCNPX simulations of neutron spectra at different longitudinal positions (at a radial distance $R = 3$ cm, «Pb/U» set-up). For better view, the values at 12.5 cm are multiplied by a factor of 2, the values at 50 cm are multiplied by a factor of 200

18

protons in a beam. The number of incident protons in performed simulations was from $5 \cdot 10^5$ up to $8 \cdot 10^6$.

Apparently from Fig. 26 the energetic spectrum is harder at the end of the target than at its beginning. Qualitatively, we drew the same conclusions from experimental results, see Fig. 24. Quantitatively, while the ratio of neutron flux density with energy of 0.15 to neutron flux density with energy of 550 MeV is $2 \cdot 10^6$ at the target forehead, this ratio is $4 \cdot 10^4$ at its end. On the other hand, the shape of the spectrum at a longitudinal distance of 12.5 cm is very similar to the shape of the spectrum at the end of the target (the ratio of neutron flux density with energy of 0.15 to 550 MeV is $6 \cdot 10^4$ at distance of 12.5 cm).

4. COMPARISON BETWEEN EXPERIMENT AND SIMULATION

The simulations describe the shape of the spatial distribution of yields of radioactive nuclei in activation detectors quite well until the distance of 45 cm from the beginning of the target. The maximum difference in absolute values is about 25%. Beyond 45 cm, the simulations underestimate the yields in both experiments and the ratio of experimental values to the simulated ones reaches two. The simulation underestimates the experiment also in the radial distance, see Figs. 27, 28, 29.

The range of 885 MeV protons in lead is about 46 cm, hence the primary proton beam should ceased out behind that point. The same holds for secondary protons produced from primary spallation reactions, as their energy is not higher than the energy of corresponding primary proton. It looks like neutron field in simulations dies close before the end of the target, while in the reality neutrons
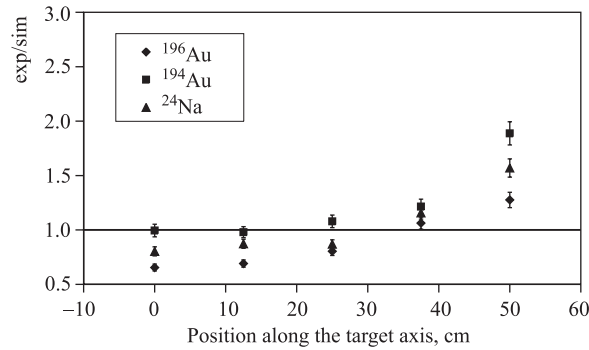

Fig. 27. Comparison of the experimental yields of ^{194}Au, ^{196}Au, ^{24}Na versus the yields from the MCNPX simulation (longitudinal distribution on «Pb/U» set-up)
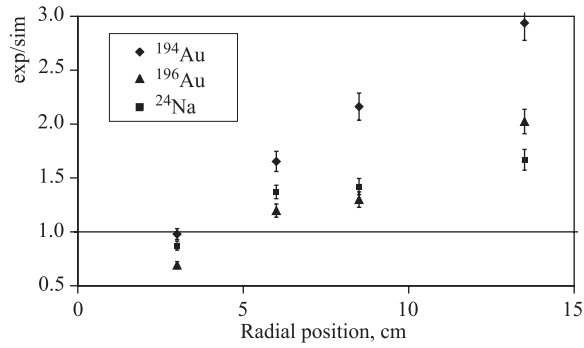
19

Fig. 28. Comparison of the experimental yields of ^{194}Au, ^{196}Au, ^{24}Na versus the yields from the MCNPX simulation (radial distribution on «Pb/U» set-up)
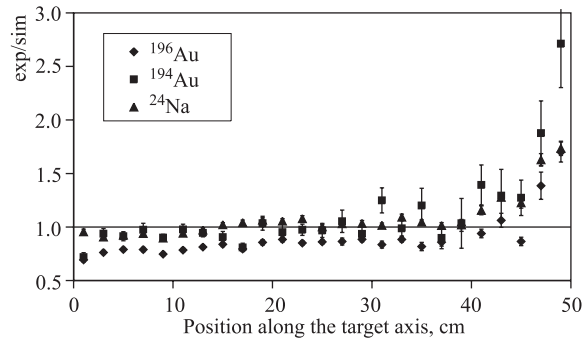

Fig. 29. Comparison of the experimental yields of ^{196}Au, ^{194}Au, ^{24}Na versus the yields from the LAHET+MCNP simulations («Pb» set-up)
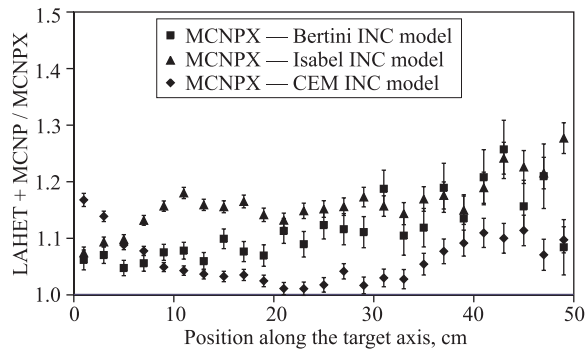

Fig. 30. Comparison of the LAHET+MCNP and MCNPX (Bertini, Isabel, and CEM INC models) simulations of yields of ^{24}Na (longitudinal distribution on «Pb» set-up)

20

survive beyond the end of the target. Therefore, we concluded that the simulations underestimate the development of the shower produced by high-energy secondary neutrons and their interactions in the target.

Although the range of 1.5 GeV protons is greater than the length of used target, one can see a similar trend in this case – the simulation underestimates the experimental yields in foils at the end of the target as well (Fig. 27). However, the deviation form unity is slightly lower than in 885 MeV case and it starts sooner.

As the last step, the simulations of 885 MeV experiment were performed by the MCNPX code with Bertini, Isabel, and CEM INC models. Isabel, in contrast to Bertini, allows collisions between cascade nucleons and describes more realistic, by up to 16 density steps, the shape of nuclear potential. CEM is improved Dubna Cascade-Exciton Model [28], which uses 7 density steps and Modified Exciton Model (MEM) of pre-equilibrium decay. These new values calculated by MCNPX code were compared with values obtained by a combination of the LAHET+MCNP codes, see Fig. 30. None of the models used in MCNPX changed significantly the simulated yields. Moreover, these changes do not go in the direction needed. Therefore, new code is also not able to explain the discrepancy between the simulation and the experiment at the end of the target.

CONCLUSIONS

We studied the neutron production in the reactions of relativistic protons with energies of 885 MeV and 1.5 GeV in a thick lead target with and without uranium blanket, surrounded by moderator. The shape and the intensity of the neutron field were measured by the neutron activation analysis method. We found out in both experiments that the maximum intensity of the fast neutron field produced in the spallation target is located in the region between 7–11 cm from the target forehead. We also found out that the energetic spectrum becomes harder at the end of the target.

We reached good qualitative agreement between experimental data and simulations for high-energy neutron production. The simulations underestimate production of isotopes in foils placed at the end of the target and beyond the blanket. It can indicate a difference between the development of the secondary-particle shower and the fission in uranium blanket in the real experiment, and in the model used in the simulations. The difference between the values from LAHET 2.7 + MCNP4B and MCNPX 2.3.0 is not significant in our case.

A further detailed analysis of the sources of the differences between experiment and simulation is in progress. We also plan to carry out a comparison with experiments with various beam energies (0.7–2.0 GeV), beam particles

(deuterons), target materials (Pb+Bi eutectics), and set-ups (extension of Pb target and U blanket).

REFERENCES

1. *Bowman C. D. et al.* Nuclear Energy Generation and Waste Transmutation Using an Accelerator-Driven Intense Thermal Neutron Source // Nucl. Instr. Meth. Phys. Res. A. 1992. V. 320. P. 336–367.

2. *Henzl V. et al.* Transmutation of ^{129}I with High Energy Neutrons Produced in Spalla-tion Reactions Induced by Protons in Massive Target // Proc. of the Intern. Conf. on Nuclear Data for Science and Technology «ND 2001», Tsukuba, 7–12 October, 2001. J. Nucl. Sci. Tech. 2001. V. 2. P. 1248–1251.

3. *Krivopustov M. I. et al.* First Experiments on Transmutation Studies of ^{129}I and ^{237}Np Using Relativistic Protons of 3.7 GeV // J. Radioanal. Nucl. Chem. 1997. V. 222. P. 267–270.

4. *Krivopustov M. I. et al.* First Experiments with a Large Uranium Blanket within the Installation «Energy plus Transmutation» Exposed to 1.5 GeV Protons // Kerntechnik. 2003. V. 68. P. 48–54.

5. *Kugler A., Wagner V., Filip C.* Experimental Study of Neutron Fields Produced in Proton Reactions with Heavy Targets // Proc. of the 3rd Intern. Conf. on Accelerator Driven Transmutation Technologies and Applications «ADTTA'99», Prague (Průhonice), 7–11 June, 1999; http://www.fjfi.cvut.cz/con_adtt99/papers/We-O-E18.pdf.

6. *Prael R. E., Lichtenstein H.* User Guide to LCS: The LAHET Code System. LANL report LA-UR-89-3014. Los Alamos, 1989.

7. *Briesmeister J. F.* MCNP – A General Monte Carlo N-Particle Transport Code Version 4B. LANL report LA-12625-M. Los Alamos, 1997.

8. *Waters L. S.* MCNPX User's Manual, Version 2.3.0. LANL report LA-UR-02-2607. Los Alamos, 2002.

9. *Chadwick M. B. et al.* Cross-Section Evaluations to 150 MeV for Accelerator-Driven Systems and Implementation in MCNPX // Nucl. Sci. Eng. 1999. V. 131. P. 293–328.

10. Stopping Powers and Ranges for Protons and Alpha Particles. International Commission on Radiation Units and Measurememnts, Inc. Report No. 49. 1993. [Tables and graphs of these data are available at http://physics.nist.gov/PhysRefData/Star/Text/PSTAR.html]

11. *Kovalenko A. D.* Nuclotron: First Beams and Experiments at the Superconducting Synchrotron in Dubna. http://sunhe1.jinr.ru/page/nucl/nuclotron.html

12. *Agapov N. N., Kovalenko A. D., Malakhov A. I.* Nuclotron: Main Results and Perspectives. http://lhe.jinr.ru/english/nuclotron/nuclotron.htm

13. *Krivopustov M. I. et al.* Investigation of Neutron Spectra and Transmutation of ^{129}I, ^{237}Np and Other Nuclides with 1.5 GeV Protons from the Dubna Nuclotron Using the Electronuclear Installation «Energy plus Transmutation». JINR Preprint E1-2004-79. Dubna, 2004.

14. Qtool: Calculation of Reaction Q-values and Thresholds. http://t2.lanl.gov/data/qtool.html

15. *Audi G. et al.* The NUBASE Evaluation of Nuclear and Decay Properties // Nucl. Phys. A. 1997. V. 624. P. 1–124.

16. Modular Pulse-Processing Electronics and Semiconductor Radiation Detectors. EG&G Ortec Catalog. 1997/8. Oak Ridge, TN 37831-0895.

17. *Frána J.* Program DEIMOS32 for Gamma-Ray Spectra Evaluation // J. Radioanal. Nucl. Chem. 2003. V. 257, No. 3. P. 583–587.

18. *De Corte F.* The k0-Standardization Method. A Move to the Optimization of Neutron Activation Analysis // Ryksuniversiteit Gent: Facultei Van de Wetenschappen, 1986.

19. *Hnatowicz V.* Handbook of Nuclear Data for Neutron Activation Analysis. Evaluation of Gamma-Ray Spectra. Czechoslovak Atomic Energy Commission, Nuclear Information Centre. Prague, 1986.

20. *Firestone R. B.* Table of Isotopes. 8th Edition. 1998.

21. *Bertini H. W.* Low-Energy Intranuclear Cascade Calculation // Phys. Rev. 1963. V. 131. P. 1801.

22. Evaluated Nuclear Reaction Data File (ENDF). http://www.nndc.bnl.gov/endf.

23. Experimental Nuclear Reaction Data (EXFOR/CSISRS). http://www.nndc.bnl.gov/exfor.

24. *Wan J. S. et al.* Monitor Reactions in Al-Foils for High Energy Proton Beams Bombarding a Thick Target // Nucl. Instr. Meth. Phys. Res. B. 1999. V. 155. P. 110–115.

25. *Bennliure J.* New Data and Monte Carlo Simulations on Spallation Reactions Relevant for the Design of ADS // Proc. of the 6th Information Exchange Meeting «Actinide and Fission Product Partitioning and Transmutation», Madrid, 11–13 December, 2000. P. 355–366.

26. *Aleksandrov Yu. V. et al.* (P, X) Reactions Cross Sections in Aluminium at Medium Energy Protons // Proc. of the Conference on Nuclear Spectroscopy and Nuclear Structure, Moscow, 1996;
Aleksandrov Yu. V. et al. Production Cross Section for Radioactive Nuclides in Copper Target Bombarded by 660 MeV Protons // Ibid.;
Jaszuk C. M., Kaminski W. A. Nuclear Phenomenology and Neural Networks // Ibid.

27. *Michel R. et al.* Nuclide Production by Proton-Induced Reactions on Elements ($6 \leqslant Z \leqslant 29$) in the Energy Range from 800 to 2600 MeV // Nucl. Instr. Meth. Phys. Res. B. 1995. V. 103. P. 183–222.

28. *Gudima K. K., Mashnik S. G., Toneev V. D.* Cascade-Exciton Model of Nuclear Reactions // Nucl. Phys. A. 1983. V. 401. P. 329–361.